Joule

Article

Enhancing water and oxygen transport through electrode engineering for AEM water electrolyzers

Graphical abstract

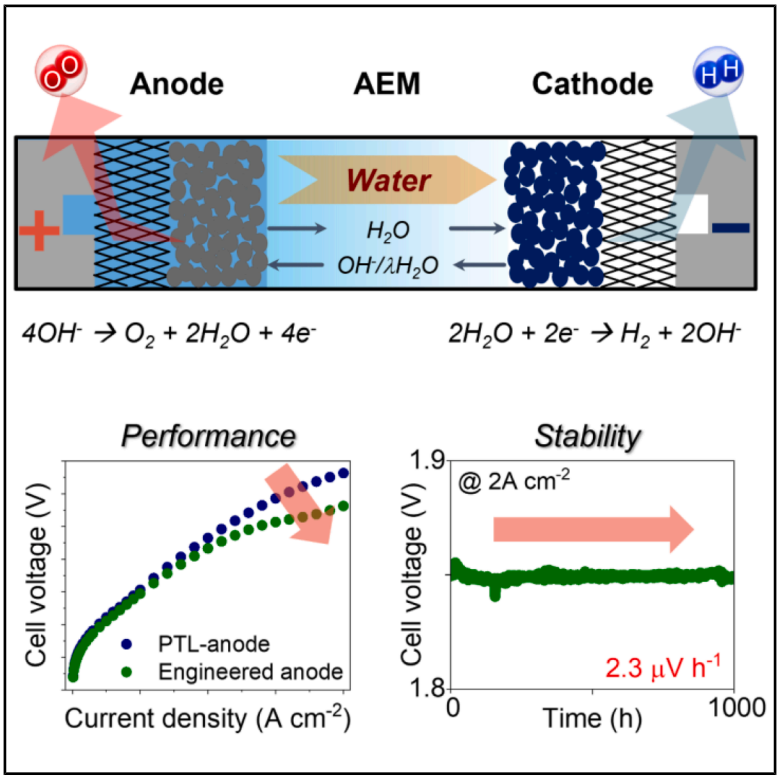

Highlights

- Identify critical role of water back-diffusion in AEMWEs
- Unravel electrode structural effects on efficiency losses in AEMWEs
- Identify ink recipes for scalable electrode manufacturing
- Demonstrate durable operation of AEMWEs

Authors

Rito Yanagi, Patrick Yang, Andrew W. Tricker, ..., Sarah A. Berlinger, Iryna V. Zenyuk, Xiong Peng

Correspondence

xiongp@lbl.gov

In brief

Addressing the convoluted water and oxygen transport phenomena in anion-exchange membrane water electrolyzers (AEMWEs) remains a considerable challenge, which hinders further efficiency and durability improvement. Correspondingly, we utilize a series of in cell, *in situ*, and *operando* measurements to investigate how electrode structure can impact species transport and resultant performance in AEMWEs. The results guide us to design ink recipes with preferred rheology, allowing for lost-cost and scalable manufacture of electrodes with enhanced transport features, which ultimately achieves outstanding electrolysis performance and durability.

Yanagi et al., 2025, Joule 9, 102001
July 16, 2025 © 2025 The Author(s). Published by Elsevier Inc.
https://doi.org/10.1016/j.joule.2025.102001

CellPress

Joule

CellPress
OPEN ACCESS

Article

Enhancing water and oxygen transport through electrode engineering for AEM water electrolyzers

Rito Yanagi,[1] Patrick Yang,[2,3] Andrew W. Tricker,[1] Yu Chen,[4] Mary C. Scott,[4] Sarah A. Berlinger,[1] Iryna V. Zenyuk,[2,3] and Xiong Peng[1,5,*]

[1]Energy Storage and Distributed Resources Division, Lawrence Berkeley National Laboratory, Berkeley, CA 94720, USA
[2]Department of Chemical and Biomolecular Engineering, University of California, Irvine, Irvine, CA 92697, USA
[3]National Fuel Cell Research Center, University of California, Irvine, Irvine, CA 92697, USA
[4]National Center for Electron Microscopy, Molecular Foundry, Lawrence Berkeley National Laboratory, Berkeley, CA 94720, USA
[5]Lead contact
*Correspondence: xiongp@lbl.gov
https://doi.org/10.1016/j.joule.2025.102001

CONTEXT & SCALE Anion-exchange membrane water electrolyzers (AEMWEs) potentially combine the benefits of low cost and high efficiencies from incumbent water electrolysis technologies. While tremendous efforts have been made in advancing material properties (e.g., developing novel catalyst materials or polymer membranes), large-scale deployment of AEMWEs for hydrogen production has not been achieved, primarily due to performance and durability limitations, especially under industrially relevant conditions (such as at high current and dry-cathode operations). This study investigates sources of efficiency loss and identifies the critical role of water back-diffusion in affecting species transport and electrode kinetics under representative electrode architectures and feeding configurations. The experimental observations are complemented with extensive *in situ* and *operando* characterizations. To achieve scalable fabrication of electrodes with enhanced transport features, a key additive is selected to fine tune ink properties. By doing so, the correlation among catalyst ink rheology, electrode structure, and AEWME performance can be established and demonstrated in this study. Our rational electrode design strategy allows for drastic improvement in AEMWE efficiency and durability.

SUMMARY

Anion-exchange membrane water electrolyzers (AEMWEs) can accelerate the deployment of more efficient and affordable hydrogen production solutions. Here, electrode structure is shown to affect water back-diffusion and oxygen transport, which, in return, governs overpotential behaviors in AEMWEs. Measurements indicate that electrode with copious catalytic sites produces water close to the AEM, creating a higher water gradient and driving water back-diffusion, which improves membrane hydration and mass transport. *In situ* measurement reveals a high pH gradient near the anode surface, which affects anode kinetics. *Operando* measurement shows reduced oxygen accumulation when decoupling oxygen production and transport on anode. Catalyst ink rheology and stability are tuned with additives to realize scalable fabrication of electrodes with enhanced transport features, allowing AEMWE to operate at 2 A cm^{-2} for over 1,000+ h at a 2.3 μV h^{-1} degradation rate. Analysis during and post-durability provides insights into degradation mechanisms. This work demonstrates an electrode design strategy for efficient and durable AEMWEs.

INTRODUCTION

Achieving low-cost hydrogen production from abundant resources (such as water) is essential for enhancing energy resilience and security thanks to the versatile role that hydrogen can play in many industrial applications. For instance, hydrogen can be used as storage media for grid balancing,[1] feedstocks for ammonia and steel production, or heavy oil refining,[2,3] and fuel to power fuel cells for heavy-duty transportation.[4,5] It is projected that the global hydrogen demand will increase from 90 to 500 Mtpa (million metric tons per annum) by 2050.[6] Thus, scaling up hydrogen production with improved efficiency and durability

This is an open access article under the CC BY license (http://creativecommons.org/licenses/by/4.0/).

will be critical. Among many technologies, low-temperature electrolysis (LTE) of water can offer a promising pathway to achieve hydrogen production at scale.[7]

Incumbent LTE technologies include liquid alkaline water electrolyzers (LAWEs) and proton-exchange membrane water electrolyzers (PEMWEs). LAWEs utilize inexpensive cell components and operate in highly concentrated hydroxide electrolyte (~7 M).[8,9] Despite low capital expenditures and extended longevity (up to ~20 years) in steady-state operation, LAWEs suffer from low efficiencies and high gas crossover due to use of porous separators.[8,10] Dynamic operation of LAWE stacks also raises durability concerns, which leads to electrode degradation due to reverse currents.[11,12] On the other hand, PEMWE achieves much higher current density and energy efficiency and can handle dynamic operation owing to its compact zero-gap membrane-electrode-assembly (MEA) design. However, highly corrosive anode environment requires platinum-coated cell components and iridium-based oxygen-evolution reaction (OER) catalysts,[13,14] which induces high capital costs and poses potential supply chain bottleneck for large-scale (gigawatt to terawatt) deployment.[13,15]

Anion-exchange membrane water electrolyzer (AEMWE), as an emerging water electrolysis technology, is in a unique position to leverage benefits of both LAWEs and PEMWEs.[16] AEMWEs employ a zero-gap MEA design which can achieve high energy efficiency at high currents and potentially handle dynamic operation thanks to feeding with dilute electrolytes (KOH; ~1.0 M or less) or pure water.[17,18] The alkaline environment in AEMWEs enables usage of abundant and inexpensive catalyst materials and cell components.[19] Despite the fact that AEMWEs could bring more affordable and efficient hydrogen production solutions, a few challenges persist in hindering AEMWE from large-scale deployment.

One of the main challenges comes from limited durability demonstration at industrially relevant conditions such as under high current density and dry-cathode operation. A well-known factor that restricts AEMWE longevity is the oxidative instability of anion-exchange ionomer binder under highly oxidizing and alkaline conditions, leading to performance decay due to loss of ionic conductivity and catalyst delamination.[20] To circumvent these issues, various mitigation strategies have been developed. Recent studies have demonstrated catalyst-layer-free electrodes as a promising strategy to achieve excellent performance and stability.[21–23] Tricker et al. have used an electro-active stainless steel (S.S.) porous-transport layer (PTL) as anode and achieved a degradation rate of only 5 $\mu V\ h^{-1}$ at 2 A cm^{-2} for 600 h.[21] Magnier et al. have examined various commercial S.S. as OER electrodes in alkaline media and found that these Fe-Ni-based alloys are highly active OER catalysts regardless of initial Fe and Ni composition.[24] Beyond commercially available electrodes, Li et al. developed a seed-assisted heterogeneous-nucleation method to synthesize and anchor nickel-iron-based nanoparticles onto PTLs and achieved high current density (e.g., 7.35 A cm^{-2} at 2 V) and an impressive durability for ~15,000 h at 1 A cm^{-2} in half-cell measurement.[23] Even though PTL-anodes perform well with KOH supporting electrolytes, adding an anode catalyst layer will further improve AEMWE performance. Previous numerical simulation indicates that anode region that is in proximity to the AEM will be preferentially utilized and higher electrochemical active surface area (ECSA) can reduce bubble coverage on electrode surface.[21] However, a stable anode catalyst layer is needed before this strategy can come to fruition.

Besides, operating AEMWE under dry-cathode mode is desirable under industrial settings, as it can streamline balance-of-plants with less electrolyte pumps and pipes, simplify cathode pressurization during differential pressure operation and avoid electrolyte mixing for less gas crossover, therefore reducing capital cost and levelized cost of produced hydrogen. In contrast to PEMWE where water is consumed by OER and migrates along with protons from anode to cathode, water is consumed by hydrogen-evolution reaction (HER) and dragged away from cathode by OH^- and produced by OER on anode in AEMWE.[25] Therefore, water management is critical when operating AEMWE under dry-cathode condition to maintain high performance, especially under high current density. Previous studies have investigated effects of membrane thickness,[26] cathode ionomer water uptake,[27,28] and anode catalyst distribution[29] on enhancing water content and minimizing cathode dry-out. Since water gradient is naturally created by OER and HER on each side of AEMWE, it is possible that water gradient can be altered by manipulating the location of each reaction zone through electrode design to promote water back-diffusion for better performance under dry-cathode operation.

Here, strategies on electrode design are presented to address the abovementioned AEMWE durability and performance challenges particularly under dry-cathode operation. 3-electrode MEA measurements are leveraged to decouple kinetic, ohmic, and transport overpotentials in AEMWEs with two typical anodes, including using electro-active PTL as anode (defined as PTL-anode) and catalyst layer-coated PTL as anode (defined as porous-transport electrode [PTE]). The beneficial role of PTEs in enhancing water back-diffusion in dry-cathode operation is elucidated by the combination of detailed voltage breakdown analysis and local pH measurement using *in situ* Raman spectroscopy. To realize high uniformity and minimize catalyst ink intrusion during PTE fabrication, catalyst ink recipes are developed to optimize rheology and stability. Finally, industrial relevance of electrode design is evaluated by investigating the cell performance and durability of scaled-up PTEs under high current density.

RESULTS

Effects of electrode and feeding modes on AEMWEs

Since bare S.S. PTL has been demonstrated as an efficient and stable anode for AEMWE when feeding KOH as supporting electrolyte.[21] It is used as the PTL-anode in this study and compared with PTE using the same S.S. PTL coated with Co_3O_4 catalyst layer (Figure 1A vs. Figure 1C). As shown in Figure 1A, one clear observation is that for PTL-anode, although a fairly good performance is achieved under both-fed condition (2.16 V at 4 A cm^{-2}), there is a significant voltage loss between 1 and 4 A cm^{-2} when operated under dry-cathode mode. The voltage loss trend, however, is not observed for PTE cell (Figure 1C), which has an even lower cell voltage under dry-cathode compared

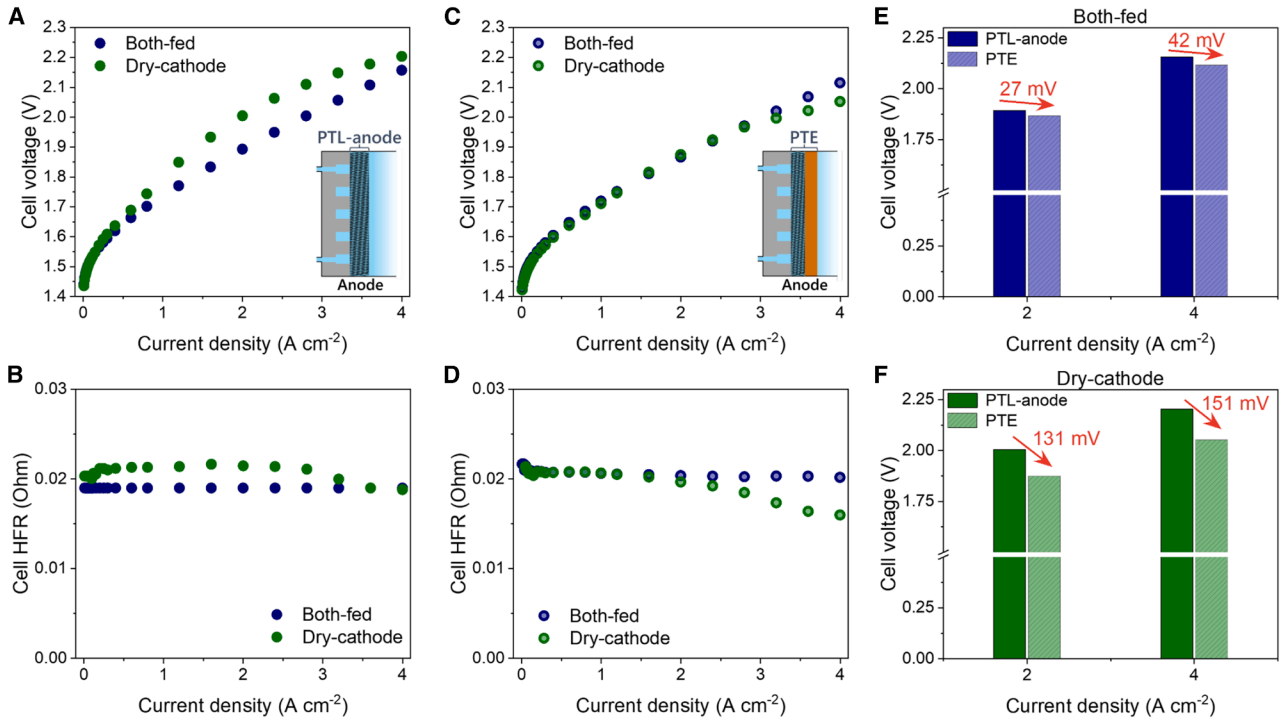

Figure 1. Representative performance comparison between both-fed and dry-cathode feeding modes for S.S. PTL-anode and PTE in AEMWEs

(A and B) (A) Polarization curve and (B) HFR of S.S. PTL-anode in AEMWE.

(C and D) (C) Polarization curve and (D) HFR of PTE as anode in AEMWE.

(E and F) Cell voltage comparison between S.S. PTL-anode and PTE under (E) both-fed and (F) dry-cathode feeding mode in AEMWEs. Inset in (A) and (C) show schematics of the anode in each AEMWE. Active area: 5 cm^2. Anode PTE: Co_3O_4 4.4 ± 0.26 mg cm^{-2}. Cathode GDE: 0.6 ± 0.1 mg_{Pt} cm^{-2}. Membrane: 80 μm PiperION-A. Temperature: 80°C. Electrolyte: 0.5 M KOH.

with both-fed conditions at above 3 A cm^{-2}. As a result, a voltage discrepancy that is dependent on feeding mode can be observed when comparing performance between PTL-anode and PTE (Figure 1E vs. Figure 1F). For instance, at 2 and 4 A cm^{-2}, PTE cell exhibits voltages that are 27 and 42 mV lower, respectively, than those of PTL-anode cell under both-fed conditions (Figure 1E), while under dry-cathode condition, the PTE cell exhibits voltages that are 131 and 150 mV lower, respectively, than those of PTL-anode cell (Figure 1F). These results highlight the importance of anode catalyst layer in promoting AEMWE performance, particularly under dry-cathode operation. Since water back-diffusion is critical in determining dry-cathode performance, we hypothesize that anode catalyst layer could potentially affect AEMWE water dynamics by promoting water back-diffusion.

High-frequency resistances (HFRs) were also measured at different currents to estimate ohmic resistance for these two types of anodes in AEMWEs. In PTL-anode cell, slightly higher HFRs are observed under dry-cathode compared with both-fed condition (Figure 1B). In contrast, HFRs in PTE cell have similar values between both-fed and dry-cathode conditions up to ~2 A cm^{-2} (Figure 1D). Since HFR measurements at different feeding conditions were conducted using the exact same cell for a given anode, HFR discrepancy should primarily represent difference in AEM hydration level and its ionic conductivity. Therefore, these results indicate that AEM dehydration and ionic conductivity loss in dry-cathode operation could be mitigated in PTE cells. When compared with both-fed conditions, where HFRs remain identical at different current densities, a clear descending trend of HFRs as increase of current density is observed between 2 and 4 A cm^{-2} for both PTL-anode and PTE cells under dry-cathode condition. This observation suggests that while being counterintuitive, dry-cathode operation can enhance AEM hydration compared with both-fed conditions when current density increases. We attribute this feature to higher water gradient between anode and cathode at higher current density, which promotes water back-diffusion and results in better AEM hydration.

Decoupling anode and cathode polarization behavior

To further probe effects of water dynamics induced by electrode structure and feeding modes on AEMWE performance, 3-electrode measurements were conducted in a PTE cell to deconvolute polarization and impedance behaviors of anode (Figures 2A and 2B) and cathode (Figures 2C and 2D). The 3-electrode measurement protocol followed a previous study[26] and was repeated at least three times to ensure consistency (Figure S1). During each measurement, reference electrode sensing point was maintained near the AEM and cathode interface, therefore HFRs measured for anode side represented most of the full cell ohmic resistances.

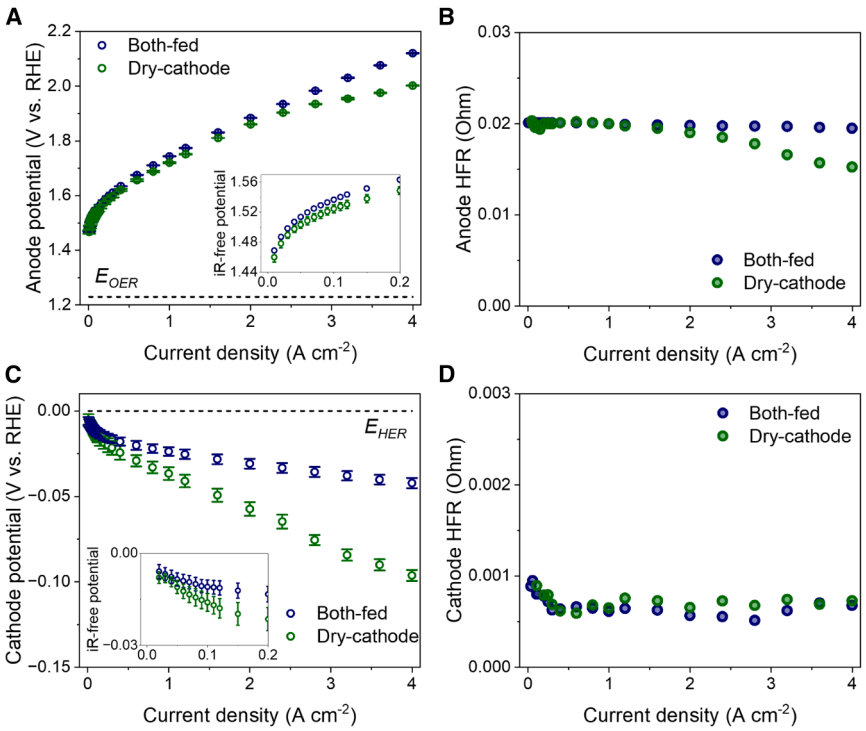

Figure 2. Voltage breakdown of AEMWE using PTE as anode by 3-electrode MEA measurements

Anode (A) polarization curve and (B) HFR. Cathode (C) polarization curve and (D) HFR. Dashed line in (A) and (C) represents the thermodynamic equilibrium potential for OER and HER at measured condition, respectively. Active area: 5 cm^2. Anode PTE: Co_3O_4 4.4 ± 0.26 mg cm^{-2}. Cathode GDE: 0.6 ± 0.1 mg_{Pt} cm^{-2}. Membrane: 80 μm PiperION-A. Temperature: 80°C. Electrolyte: 0.5 M KOH. Error bars represent the standard deviation of three measurements.

While cathode HFRs remain identical between two feeding conditions (Figure 2D), cathode overall overpotential is higher under dry-cathode condition (Figure 2C). A detailed overpotential breakdown indicates that cathode kinetics dominates cathode voltage loss under dry-cathode condition, with 18 mV higher compared with both-fed condition at 4 A cm^{-2} (Figure S2). This is also seen in the 3-electrode AEMWE measurement using PTL-anode (Figures S3–S5). The specific activity of cathode catalyst (Pt/C) for HER is not expected to change under these two feeding conditions, thus, kinetic overpotential discrepancy is likely due to a loss of ECSA when supporting electrolyte is not fed to cathode. This is supported by a reduction in both the Pt ECSA and cathode double layer capacitance under dry-cathode compared with both-fed conditions (Figure S6). The residual overpotential of cathode, which mainly represents mass transport loss, is also quantified. Even though cathode residual overpotentials are higher in dry-cathode compared with both-fed condition for both the PTE and PTL-anode cells (Figures S2 and S5), PTE cell demonstrates significantly lower cathode residual overpotential than that of the PTL-anode cell under dry-cathode operation (Figure S7F), as well as lower cathode ohmic overpotential (Figure S7D). For instance, PTE cell shows a reduction of 42 and 12 mV in ohmic and residual overpotential at 4 A cm^{-2}, respectively, which further supports the hypothesis of enhanced water supply to cathode through back-diffusion in PTE cell.

It is worth noting that both PTE and PTL-anode show different polarization behaviors between both-fed and dry-cathode feeding conditions (Figures 2A and S4). This is unexpected as dry-cathode operation typically affects cathode water supply as shown by higher cathode residual overpotential, and anode is not to be impacted since it is always fed with the same electrolyte. In PTL-anode cell where anode performance is impeded by dry-cathode compared with both-fed operations, anode has identical OER kinetic loss and ohmic overpotential under both feeding conditions (Figures S5A and S5B), and the inferior performance under dry-cathode operation is solely due to higher anode residual overpotential (Figure S5C). On the contrary, when using PTE as anode, lower anode overpotential observed under dry-cathode operation is due to a combination of lower HFRs (Figure 2B), enhanced electrode kinetics (Figures 2A inset and S2B), and reduced residual overpotential (Figure S2C). The difference between PTE and PTL-anode is that a catalyst layer is closely located near AEM, therefore during operation, this catalyst layer will be preferentially utilized for OER due to the proximity of AEM. It should also be noted that water is produced by OER (defined as OER-water) in two pathways: direct conversion of hydroxide into water and release of electro-osmotically dragged water by consumption of hydroxide. In the case of PTE as anode, OER-water will be more closely located near AEM than that of PTL-anode. As a result, a higher water gradient is created across AEM therefore drives up water back-diffusion for PTE compared with PTL-anode in AEMWEs. As current density increases, water gradient is further enhanced, facilitating greater water back-diffusion. This explains the lower ohmic resistance of PTE compared with PTL-anode and descending HFR trend as increase of current due to better AEM hydration.

Visualizing anode oxygen distribution in AEMWEs

It is also worth noting that PTE anode shows lower residual overpotential compared with that of PTL-anode under dry-cathode (Figure S7C) and both-fed conditions (Figure S8). Anode residual overpotential is primarily a combination of mass transport overpotential and ionic resistance, both of which are directly related to oxygen transport on anode. We therefore utilize *operando* X-ray computed tomography (CT) to probe oxygen bubble dynamics for both PTE and PTL-anode in AEMWEs. The *operando* technique provides cross-sectional view of AEMWE under open-circuit voltage (Figure 3A) and operating conditions (Figure 3B), of which

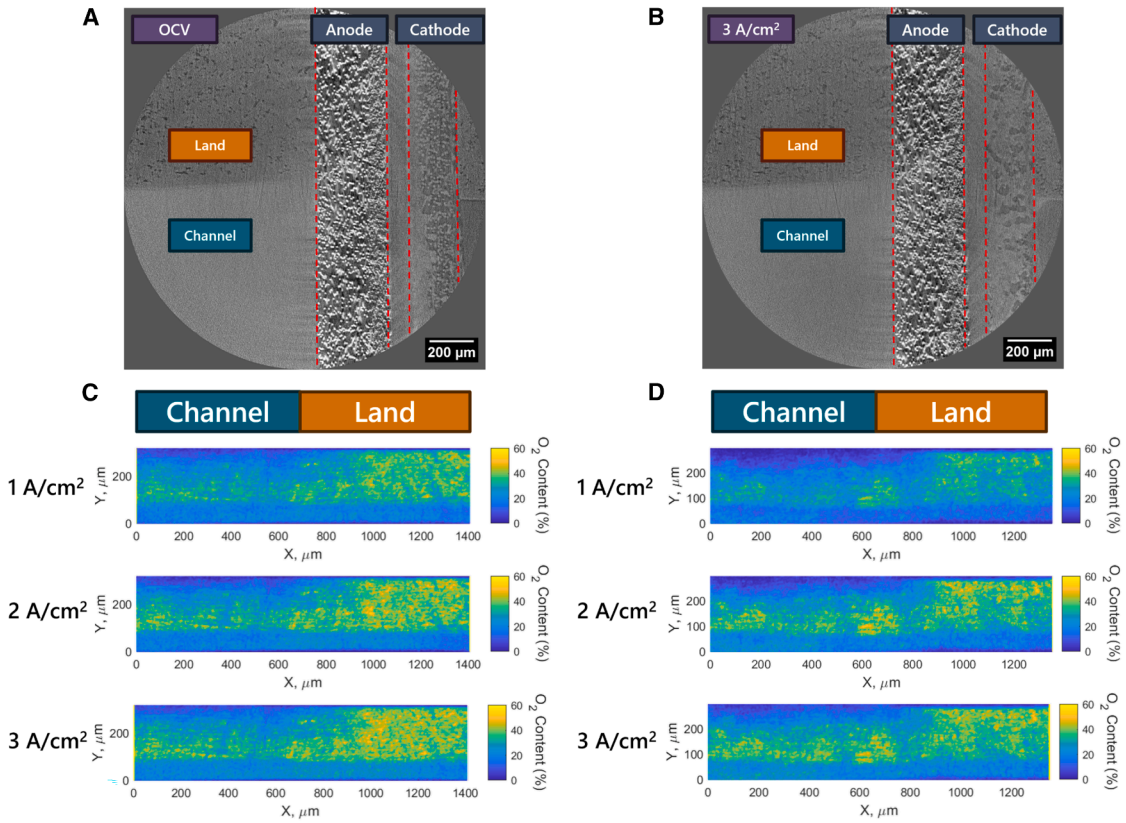

Figure 3. *Operando* X-ray CT scans of AEMWEs

(A) Open-circuit voltage (OCV) and (B) at 3 A cm^{-2}. The cross-sectional view shows the anode, cathode and AEM in between. The land and channel are from the anode flow field. The calculated oxygen content and distribution based on CT scans on anode side at 1, 2, and 3 A cm^{-2} in AEMWEs for (C) PTL-anode and (D) PTE. Y = 0 indicates the interface between anode and AEM. The O_2 content represents the ratio between volume of oxygen and volume of pores in PTL. 3 M CsOH was used as electrolyte to increase X-ray attenuation and provide better contrast. Electrolyte was only fed to anode side during measurement.

the X-ray attenuation difference allows one to estimate both oxygen content and its distribution on anode. Oxygen content represents the oxygen volumetric fraction in void space of anode.[30] As the increase of current density, a higher oxygen content is observed for AEMWEs using both PTL-anode (Figure 3C) and PTE (Figure 3D). Besides, a higher oxygen content is observed under flow field land than that under flow field channel, owing to additional in-plane transport resistance for under-land oxygen bubble to escape. In comparison, anode side of PTE cell shows a lower level of oxygen accumulation than PTL-anode at the same current density, despite the same batch of PTLs were used in these cases. A lower level of oxygen accumulation indicates better electrolyte supply to anode and lower bubble-induced overpotential, which correlates well with results of lower residual overpotential from 3-electrode MEA measurements. The result also indicates that decoupling oxygen production from transport in PTLs by adding a catalyst layer is likely to induce different oxygen bubble dynamics even if the PTL material itself remains unchanged.

Probing anode local pH and its implications on electrode design

A rather unexpected observation is the improved anode kinetics under dry-cathode operation for PTE cell, which suggests promoting water back-diffusion also promotes anode OER kinetics. Near anode catalyst surface, hydroxide is being consumed and converted to OER-water. The local hydroxide concentration near anode catalyst surface is the net balance of hydroxide supply, consumption and OER-water accumulation at steady state. As the rate of hydroxide supply and consumption are relatively constant at a given current density, OER-water removal becomes essential in determining its concentration and local pH. Promptly removing produced OER-water could increase local hydroxide concentration, which leads to slightly more basic condition for anode and promotes OER kinetics. Although it is rather experimentally challenging to differentiate the OER-water and the water from aqueous electrolyte in an operating device, the result also implies that a pH gradient exists for OER on anode. When a pH gradient does not exist, removal of OER-water is not likely to impact the microenvironment on anode. To verify this hypothesis, we used *in situ* Raman spectroscopy to investigate interfacial pH near anode surface under OER potentials.

A pH sensitive dye molecule (pH-dye: carboxy-Snarf-1), dispersed in the electrolyte solution, was used to quantify pH near the electrode surface. This dye molecule (pK_a ~7.5) is either protonated or deprotonated depending on solution pH (Figure S9), and each form has a distinctive fluorescence peak

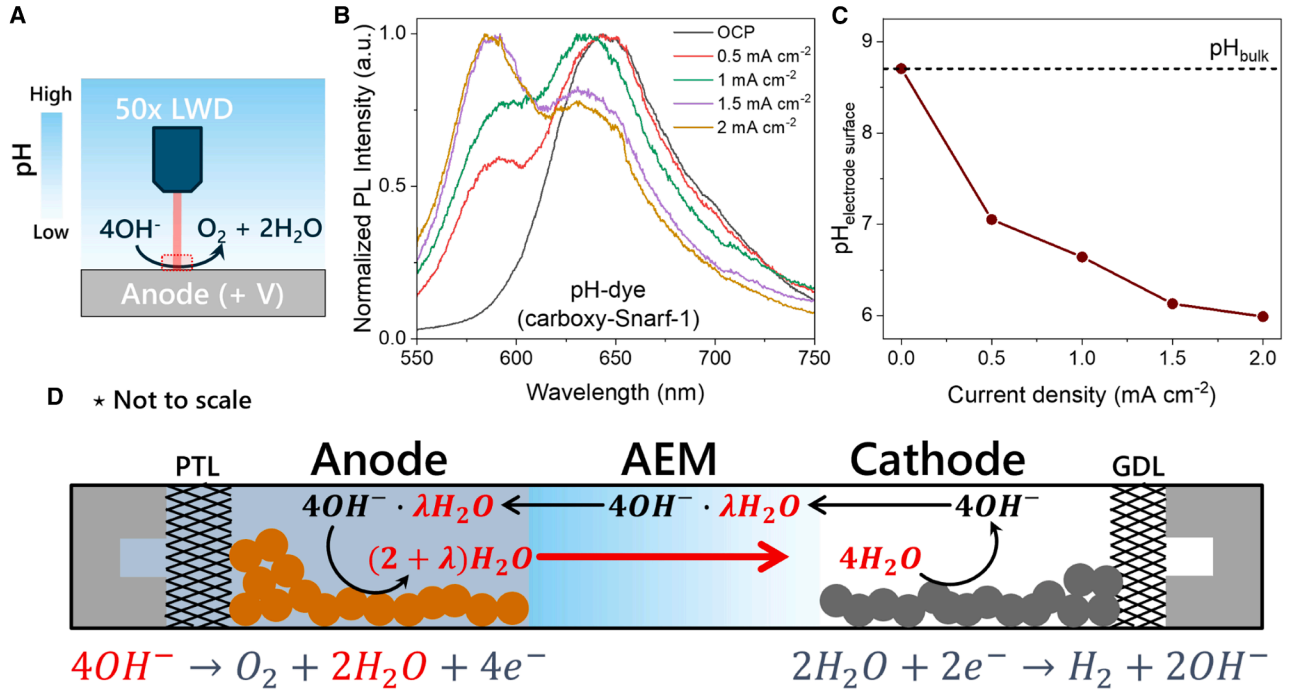

Figure 4. *In situ* Raman study on local pH near electrode surface

(A) Schematics showing the *in situ* Raman measurement.

(B) Measured photoluminescence spectra at electrode surface under different current density.

(C) Electrode surface pH calculated based on (B) under different current density.

(D) Schematics showing hydroxide and water transport in an AEMWE cell. The electrolyte was 10 μM KOH and 100 mM of $MgSO_4$ during *in situ* Raman measurement.

(590 and 640 nm, respectively). As a result, the peak at 590 nm increases with decreasing pH values. By quantifying the ratio between these two peaks, solution pH can thus be determined. A calibration in solutions with known pH values was first conducted, and the ratio between the two fluorescence peaks was then calculated and correlated with pH (Figure S10).

In the measurement, laser beam was focused on electrode surface and spatial resolution of sampling depth was controlled to be ~1 μm by tuning confocality of Raman spectrometer (Figure 4A). The measured photoluminescence spectra of electrolyte at electrode surface under different anode current density is shown in Figure 4B and their corresponding pH values are shown in Figure 4C. These results clearly show that electrode surface pH deviates from bulk solution pH and this deviation intensifies as increase of current density. In our measurements, electrode surface pH can drop as much as 3-unit values with a dilute KOH concentration of 10 μM. The pH drop is due to a combination of OH^- consumption and accumulation of OER-water in base. When OER-water can readily diffuse away due to enhanced water back-diffusion during AEMWE operation (Figure 4D), a higher anode local surface pH can potentially be achieved, which promotes anode kinetics,[31] as is seen in the voltage breakdown analysis for PTE cell (Figures 2 and S2). We note that the *in situ* measurements do not fully replicate conditions in MEA setup. The pH range of *in situ* measurements is restricted by pH sensitivity of the pH-dye, which limits initial bulk pH to be ≤9. In future studies, pH-dye with wider range of pH sensitivity is needed to represent actual MEA conditions. Nevertheless, the trend of water effects on local pH should still hold qualitatively regardless of testing conditions.

The implications from both 3-electrode MEA, *in situ* Raman and *operando* studies to electrode design are to have copious OER sites right near AEM so that OER-water can swiftly back diffuse to cathode and result in better performance for dry-cathode operation (Figure 4D). Inspired by these results, we intend to develop an electrode fabrication methodology that not only balances low cost and scalability but also produces electrodes that promote water back-diffusion and enhance performance for AEMWEs. Due to durability and swelling limitation of AEM under conditions of direct catalyst-coated membrane manufacturing,[22,32] porous-transport electrode (PTE) is often a preferred configuration for anode fabrication in AEMWEs.[26,29]

Correlating ink design with electrode structure and electrolysis performance

However, directly coating catalyst inks to porous surface of PTL for PTE fabrication can be challenging due to ink intrusion issues. This results in poor coating quality and high inhomogeneity of the PTE (Figure S11). The catalyst layer exhibits severe loss into PTL pores and PTL fibers are exposed onto the surface (Figure S11). AEMWEs built using these electrodes are likely to have limited water back-diffusion and inferior performance, which is discussed in later sections. To demonstrate more efficient and stable AEMWEs, catalyst ink properties were tuned to achieve a

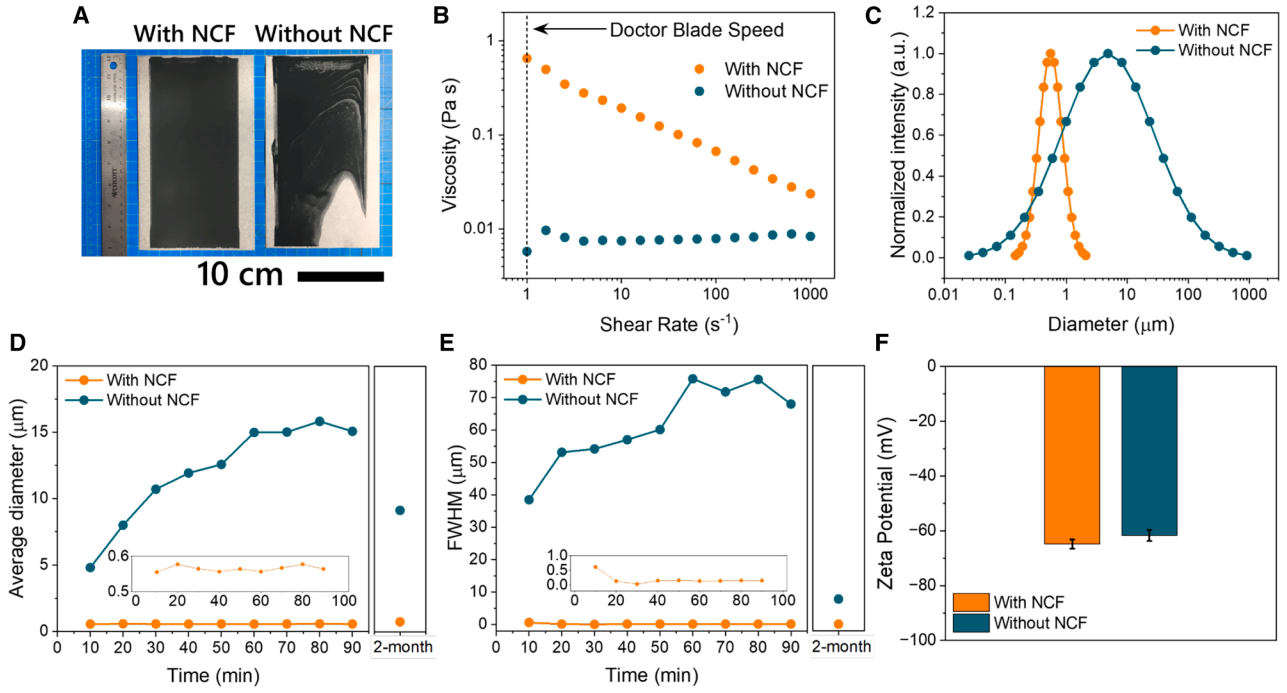

Figure 5. Characterization of catalyst ink properties with and without NCF as additive

(A) Picture of electrodes fabricated with and without using NCF as additive in catalyst inks. S.S. PTL was used as the substrate. The comparison of (B) viscosity, (C) initial particle size distribution, (D) particle diameter over time, (E) full width half maximum (FWHM) of particle size distribution over time, and (F) Zeta potential for catalyst inks with and without NCF as additive.

more uniform catalyst coating with minimum ink intrusions and catalyst loss. Besides, catalyst solid content is chosen to be at 10% of total mass of ink to increase fabrication throughput. Doctor blading is used as the coating technique owing to its low cost and high scalability to fabricate PTE. More importantly, an additive, nano cellulose fiber (NCF), was applied and found to have drastic impact on ink rheology and electrode coating quality. The selection of ink additive follows general criteria of low cost, chemical stability, environmental friendliness, and high hydrophilicity and capability to modify ink rheology.

PTEs fabricated by doctor blading (defined as DB-electrodes) using ink with NCF show improved coating quality compared with that without NCF (Figure 5A). DB-electrodes fabricated with NCF shows high coating uniformity and absence of PTL fibers from top-down view (Figure S12 vs. Figure S11), which indicates negligible ink intrusion. It should be noted that applying NCF as ink additive is the only difference during electrode fabrication; therefore, the average catalyst loading is the same between these two DB-electrodes (Figures S11 and S12). The role of NCF was further investigated to examine its impact on ink rheology. By adding NCF, viscosity of catalyst ink was drastically increased and was measured to be two orders of magnitude higher at low shear rate of 1 rotation per s (1 s^{-1}) (Figure 5B). The linear velocity at share rate of 1 s^{-1} is estimated to be the same as coating speed of doctor blading (5 m min^{-1}), which explains the phenomenon of less ink intrusion and better coating quality due to enhanced ink viscosity. Catalyst ink with NCF shows a non-Newtonian behavior of decrease in viscosity as increase of shear rate. The observed shear thinning is likely to be primarily contributed by reduction of interactions between NCF-solvent (ethanol and water in this case) instead of NCF-particle or particle-particle, as a similar behavior is also observed in NCF-added solvent mixture without catalyst particles (Figure S13).

The catalyst aggregates size distribution and stability of catalyst ink was also investigated as it would be critical in scaleup of manufacturing/coating processes. Catalyst ink with NCF shows much smaller aggregates size and narrower size distributions compared with those without NCF (Figure 5C). It can also be seen that catalyst ink with NCF exhibits nearly identical aggregate sizes overtime, indicating a relatively stable ink, while ink without NCF shows increasing sizes and more polydisperse even after just 90 min (Figures 5D and 5E). Aggregates size distributions were measured again after storing ink under continuous static condition to test shelf stability. Results show that ink with NCF can be stable even after 2 months with only a slight increase in aggregates diameter (Figures 5D and 5E). Zeta potential was quantified to determine the underlying mechanism of improved ink stability by adding NCF. Zeta potentials for inks with and without NCF show values at around negative 60 mV, suggesting Nafion binder adsorption on catalyst surface to be the dominant contributor due to its negatively charged sulfonic acid group. However, zeta potentials between these two inks show marginal difference (Figure 5F), meaning electrostatic interaction among catalyst aggregates is not the reason for improved ink stability. Instead, we postulate that the improved stability comes from a steric effect imposed by NCF fiber

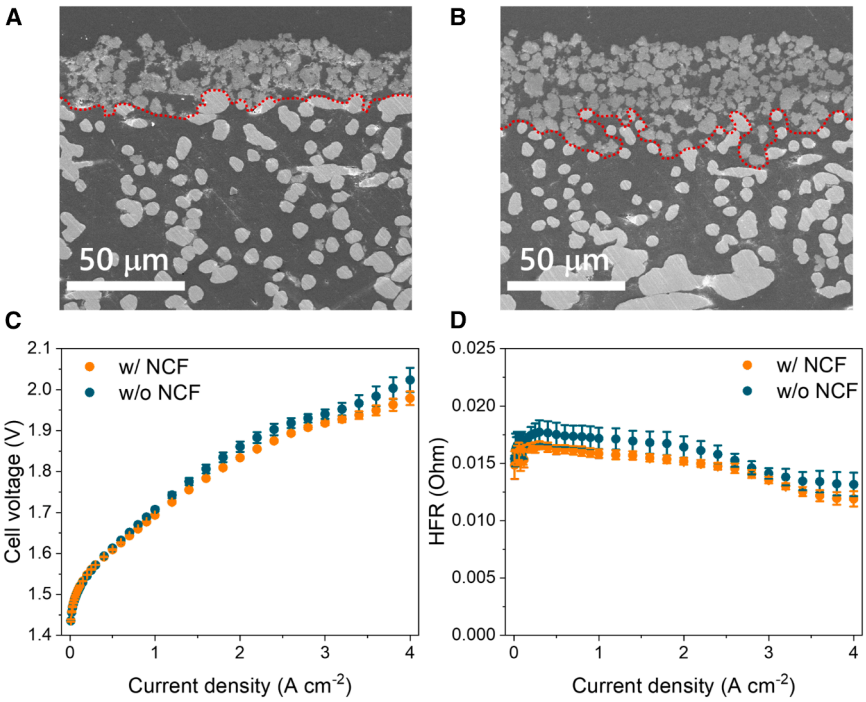

Figure 6. Impacts of NCF on electrode structure and AEMWE performance

(A and B) SEM cross-sectional images of DB-electrodes fabricated using inks (A) with NCF and (B) without NCF.

(C and D) (C) Polarization curves and (D) HFR comparison for DB-electrodes fabricated using inks with and without NCF in AEMWEs under dry-cathode operation. Red dashed lines in (A) and (B) represent a boundary between the catalyst layer and the underlying PTL and serve as guides for visualization. Active area: 5 cm^2. Anode PTE: Co_3O_4 4.4 ± 0.26 mg cm^{-2}. Cathode GDE: 0.6 ± 0.1 mg_{Pt} cm^{-2}. Membrane: 80 μm PiperION-A AEM. Temperature: 80°C. Electrolyte: 0.5 M KOH. The error bars represent the spread between three independent experiments. Error bars represent the standard deviation of three measurements.

structure. Indeed, this is supported by visualizing catalyst aggregate morphologies under transmission electron microscopy (TEM) (Figure S14). It is clearly seen that flexible fibers of NCF provide more attachment points for catalyst aggregates and allow for much smaller aggregate sizes. In catalyst inks, these fibers can act as physical barriers and provide steric hindrance among different catalyst aggregates, therefore preventing its motion and agglomeration with each other. As a result, a more stable ink with smaller aggregate size can be achieved.

DB-electrodes fabricated using catalyst inks with and without NCF were tested in AEMWEs (Figure 6). As indicated by cross-sectional images (Figures 6A and 6B), DB-electrodes fabricated using NCF ink clearly show almost no catalyst loss into pores of PTL compared with that fabricated using ink without NCF. As discussed previously, this feature is likely to create a higher water gradient across AEM, which promotes water back-diffusion during operation. AEMWEs with such electrodes have lower cell voltage than the ones without NCF under dry-cathode operation, especially at higher current density (45 mV lower at 4 A cm^{-2} in Figure 6C). This was primarily attributed to lower HFR, as shown in Figure 6D, indicating improved AEM hydration and ionic conductivity during operation. This finding further supports the benefit of electrode design in promoting water back-diffusion. Results also indicate that although NCF is not conductive, it has negligible impact on electrode conductivity given its low mass content in catalyst layer. We also examined the impact of solvent ratios (alcohol to water ratios) in catalyst inks on AEMWEs performance (Figure S15). The result indicates an optimal alcohol content of ~64 wt %, which is used in the comparative study for NCF effect. Results here present a correlation among catalyst ink properties, electrode structure, and AEMWE performance.

DB-electrode scalability and durability in AEMWEs

Scalability and durability are of critical importance toward commercialization and large-scale deployment of AEMWEs. The scalability of optimized DB-electrodes was first demonstrated by fabricating electrode at ~300 cm^2 (Figure 7A). The coating quality was examined by quantifying catalyst loading lateral variability using X-ray fluorescence measurements, which showed a standard deviation value of only 5.8 % for an area of 100 cm^2 (Figure S16). This high loading uniformity translates into consistent performance, as indicated by negligible performance discrepancy between 5 and 25 cm^2 electrodes tested in AEMWEs (Figure 7B). The locations for the 5 and 25 cm^2 electrodes used for electrochemical testing are indicated in the picture (Figure 7A).

Durability of DB-electrode was investigated by holding a 25 cm^2 AEMWE at 2 A cm^{-2} under dry-cathode condition (Figure 7C). Deionized water at room temperature was added to anolyte container approximately every 15 min to maintain steady KOH concentration, which led to periodic cell voltage oscillations due to slight temperature fluctuations. The cell voltage stabilized at ~1.85 V (Figure 7C), which was consistent with cell voltage measured by polarization curves (Figure 7B), and remained stable over 1,000 h at an average degradation rate of only 2.3 μV h^{-1}. To our knowledge, the operating condition and decay rate presented in this study represents one of the best reported AEMWE durability performances compared with literature (Table S1; Figure S17). Although cell voltage exhibited a very low degradation rate, several other factors were monitored during operation. Additionally, post-mortem analysis of cell components was performed to gain insights into the transformation occurring in AEMWE.

First, H_2 concentration in O_2 at anode outlet was periodically measured by a gas chromatography during durability test (Figure 7D). Measurements show that H_2 concentration in O_2 gradually increases and stabilizes at ~0.9 % (22.5% of lower flammability limit). As many factors can affect H_2 crossover in water electrolyzers, further studies are needed to investigate gas transport mechanism and correlate the H_2 permeation

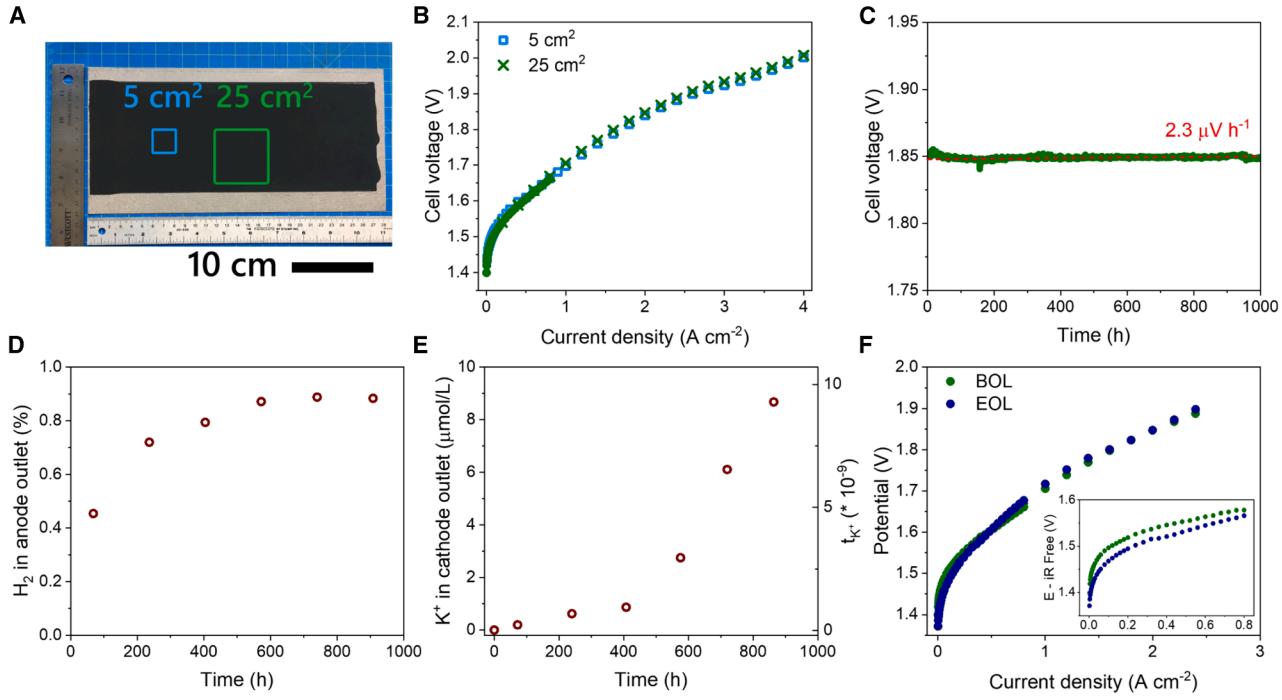

Figure 7. DB-electrode scalability and durability in AEMWEs

(A) Picture of the DB-electrodes used for testing.

(B) Polarization curves for AEMWEs with 5 and 25 cm^2 active area.

(C) Durability at 2 A cm^{-2} using an AEMWE cell at 25 cm^2.

(D) H_2 percentage in O_2 at anode outlet during durability test.

(E) K^+ concentration in cathode outlet and calculated K^+ transference number (secondary *y* axis) during durability test.

(F) Polarization curve comparison at beginning-of-life (BOL) and end-of-life (EOL). Inset shows iR-free polarization curve up to 0.8 A cm^{-2}. Active area: 25 cm^2 unless otherwise noted. Anode PTE: Co_3O_4 4.4 ± 0.26 mg cm^{-2}. Cathode GDE: 0.6 ± 0.1 mg_{Pt} cm^{-2}. Membrane: 80 μm PiperION-A AEM. Temperature: 80°C. Electrolyte: 0.5 M KOH fed to anode. During durability test, deionized water was replenished to anolyte periodically to maintain constant KOH concentration.

changes to AEM structural transformation during AEMWE operation. Thanks to enhanced water back-diffusion features enabled by electrode design, a catholyte could be collected from cathode outlet even under dry-cathode operation. Volume of catholyte was also quantified to be ~7.5 mL h^{-1} throughout the test (Figure S18), indicating no pinholes formation or membrane thinning. Catholyte compositions were analyzed using inductively coupled plasma mass spectroscopy and ion chromatography. Although K^+ crossover increases over time (Figure 7E), concentration of K^+ in catholyte remains extremely low, indicating AEM maintains its high perm-selectivity in our tests. Based on the operating current of 2 A cm^{-2} and K^+ crossover rate, K^+ transference number was determined to be $\ll 1$ (Figure 7E). This extremely low K^+ transference number further confirms that water transport from anode to cathode is mainly driven by diffusion instead of the electro-osmatic drag of K^+ in this case.

Besides, PTLs such as S.S. are prone to corrosion under anodic condition.[21,24] Thus, anode S.S. PTL morphology was examined by scanning electron microscopy (SEM) (Figure S19). Although surface of PTL was smoothened, no visible changes in morphologies such as pitting or thinning were observed. In addition, surface compositions of nickel, iron, and chromium were quantified using X-ray photoelectron spectroscopy (XPS) (Figure S20). Pristine S.S. PTL shows an iron and chromium rich surface (78% of Fe and 19% of Cr) with nickel only accounting for ~3%, while post-durability PTL shows that nickel to iron ratio increases to about 1:1, with no chromium detected. Leached-out components of PTLs can migrate away from anode and redeposit either in AEM or on cathode. XPS survey on post-durability cathode shows clear signals from Cr 2p peaks (Figure S21), indicating evident chromium redeposition. However, the intensity of Fe 2p peak is almost similar to pristine cathode (Figure S21). Iron and cobalt concentrations in catholyte remain low over 1,000 h and show negligible increase compared with the blank water samples (Figure S22). Cross-sectional image of post-durability AEM also shows no iron or cobalt oxide precipitations (Figure S23). It should be noted that a previously reported AEMWE,[21] using PTL-anode tested at similar durability condition, shows clear iron oxide precipitation near anode side of AEM (Figure S24). The discrepancy in iron oxide precipitation within AEM as well as the low Fe 2p peak intensity of post-durability cathode indicates that iron leaching from S.S. PTL can be mitigated using DB-electrodes compared with PTL-anode during AEMWE operation. This is likely since PTL in DB-electrode participates much less in anode OER compared with directly using PTL as anode, resulting in reduced PTL corrosion. Nevertheless, low-iron and

chromium-free PTLs are still recommended for further improvement in AEMWE durability. Besides, post-durability AEM thickness was measured to be around 77 μm, indicating no significant thinning after 1,000 h testing. This suggests that the observed doubling of H_2 crossover (Figure 7D) is not primarily caused by a reduction in AEM thickness, but rather possibly by structural change of AEM, as indicated by a slight increase in HFR after durability test (Figure S25).

Anode and cathode catalyst layers were also assessed through SEM imaging, which exhibited no visible catalyst layer delamination, showing excellent integrities (Figure S26). XPS on post-durability anode shows decreased peak intensity of F 1s and S 2p peaks, indicating Nafion degradation could happen to some extent in anode catalyst layer (Figures S27 and S28). However, since Nafion on anode is simply used as a binder not an ion-conducting polymer, we expect a minor chemical degradation does not impact anode ionic conductivity. We also evaluated Piperlon ionomer as anode binder in AEMWEs. Results show that despite with better initial performance compared with Nafion ionomer binder, Piperlon ionomer binder on anode suffers from durability challenges in AEMWEs due to catalyst layer delamination and ionomer oxidative instability issues (Figure S29). Anode Co_3O_4 catalyst was scratched off from electrode and prepared into specimen for TEM imaging. The electron-diffraction pattern indicates that a growing amorphous phase of Co_3O_4 during operation (Figure S30). As amorphous metal oxide often shows better OER activity compared with its crystalized counterparts,[33,34] the phase alternation explains the improved post-durability electrode kinetics, as shown by the insert of Figure 7F. A slight increase in average particle size test was observed (Figure S31), which may due to Ostwald ripening and/or particle coalescence.[35] As XPS on post-durability cathode indicates Cr and Fe deposition, cathode Pt/C catalyst was also scratched off from electrode for TEM and energy-dispersive X-ray spectroscopy (EDS) analysis (Figure S32). Results show that Fe signal is primarily associated with Pt particles, whereas Cr appears to be more randomly distributed, present on both Pt particles and the carbon surface.

The impacts of each component on AEMWE durability as mentioned above are likely to be convoluted in overall cell voltage measured by constant current hold (Figure 7C) and polarization curves before and post durability (Figure 7F). Overall, it is demonstrated that our electrode design strategy enables improved performance, stability as well as scalability for AEMWEs.

DISCUSSION

Despite electro-active PTL-anode shows promise in AEMWEs, higher voltage losses are found under dry-cathode operation due to limited water back-diffusion from anode and higher oxygen bubble-induced overpotential. It is shown that electrode with anode catalyst layer can generate OER-water near AEM, promoting water back-diffusion from anode to cathode. This is supported by 3-electrode MEA measurements, where lower HFR resulted from better membrane hydration and lower mass transport overpotential for cathode could be observed. Decoupling oxygen production by adding anode catalyst layer from oxygen transport through PTL has benefit in mitigating oxygen bubble-induced overpotential, as is evidenced by *operando* X-ray CT measurement. A rather unexpected observation shows that anode kinetics improves under dry-cathode operation, which is also attributed to prompt removal of OER-water. *In situ* Raman spectroscopy employing a pH-sensing dye molecule shows that pH at the anode surface can be significantly lower than bulk value. We argue that a robust removal of OER-water can mitigate its diluting effect and mitigate a drastic pH drop, therefore allowing anode to operate under more basic condition. To capitalize these benefits for AEMWEs, a coating strategy was developed for fabricating a uniform and homogeneous anode catalyst layer and an additive was examined to significantly tune catalyst ink properties in terms of viscosity, particle size distribution and ink stability. Using this coating method, electrodes can be fabricated at large scale ($\geq$300 cm^2) and show consistent performance between 5 and 25 cm^2 AEMWEs. Constant current hold at 2 A cm^{-2} using 25 cm^2 cell had a cell voltage of 1.85 V and a degradation rate of only 2.3 μV h^{-1} over 1,000 h. Overall, our study investigates water and oxygen dynamics of AEMWEs and demonstrates an ink and electrode design strategy to advance AEMWE under industrially relevant conditions to achieve performance and durability targets needed for commercialization.

METHODS

Chemicals and materials

Platinum on carbon (46.8 wt % Pt) was purchased from TANAKA (TKK). Cobalt oxide (Co_3O_4, >99.5%, 30–50 nm) was purchased from US Research Nanomaterials. PiperION-A membranes and ionomer dispersions (5 wt % in ethanol) were purchased in bicarbonate form from Versogen. Cellulose nanofibrils (NCF; 3 wt % in water, prepared by supermass colloider) were purchased from Celluloselab. Potassium hydroxide (85.0%) was purchased from Fisher Chemical. n-Propanol (nPA, ACS reagent, $\geq$99.5%) and ethyl alcohol (200 proof, ACS reagent, $\geq$99.5%) were purchased from Sigma-Aldrich. Nafion dispersion (D2020, 20 wt %) was purchased from Ion Power. Deionized water (18 MΩ) was produced inhouse using a Milli-Q (EMD Millipore). Carbon paper gas diffusion layers (GDLS, Toray 120, 10 wt % PTFE) and carbon black (Vulcan XC-72R) were purchased from Fuel Cell Store. Stainless-steel fiber porous-transport layers (10AL3) were purchased from Bekaert. Ethylene tetrafluoroethylene (ETFE) gasketing material was purchased from CS Hyde.

Ink preparation and electrode fabrication

Cathode

A microporous layer was first fabricated before spraying the cathode catalyst ink. For the microporous layer ink, 200 mg of carbon black and 600 mg of 20 wt % Nafion (D2020) dispersion (I:C = 0.6) were added to 16.4 g of a 1:7.2 g/g water/nPA mixture and bath sonicated in an ice bath for at least 40 min. For platinum inks, 200 mg of Pt/C and 1,070 mg of 5 wt % PiperION-A dispersion (mass ratio of ionomer to carbon = 0.5) were added to 16.4 g of a 1:7.2 g/g water/nPA mixture and bath sonicated in an ice bath for at least 40 min.

Unless otherwise stated, the gas diffusion electrodes (GDEs) were fabricated using a handheld airbrush (Iwata). The bare

GDLs were cut to a precise size with an area of 120.25 cm^2 and massed before spraying. The inks were loaded into a handheld airbrush connected to house nitrogen and deposited on the substrate over many passes until the desired loading was reached. Catalyst and microporous layer loadings were determined from the difference in the initial and final weights of the GDEs. A typical GDE has 0.6 ± 0.1 mg_{pt} cm^{-2}loading unless otherwise specified. After fabrication, either 5 or 25 cm^2 squares were cut from the fabricated GDE for AEMWE testing.

Anode

For anode inks, 1.5 g of Co_3O_4 and 750 mg of Nafion D2020 dispersion and 1.875 g of cellulose nanofibrils (NCF, 3 wt % in water) were added to 11 g of a 4:7 g/g water/ethanol mixture and mixed with a shear mixer (Silverson L5M-A) at 10,000 rpm for 30 min. The mixture was put into an ice bath during shear mixing and caped with parafilm to prevent solvent evaporation.

Unless otherwise stated, the PTEs were fabricated using doctor blade coating method with loading Co_3O_4 at 4.4 ± 0.26 mg cm^{-2}. Stainless-steel fiber porous-transport layers were cut to a size of 6 inch × 9 inch and massed before being fixed onto the doctor blade coater (MTI, MSK-AFA-III Automatic Thick Film Coater). The temperature of the coater furnace was set to 100°C and the PTL equilibrated at 50°C after 1 h. Vacuum was pulled beneath the PTL to <0.8 bar to ensure a flat surface for coating. Anode catalyst ink was squeezed onto one edge of the PTL immediately before coating at 5 m/min. The gap of the coater was set to 25 μm. The coated PTE was then dried for 30 min at 50°C. Catalyst loading was determined from the difference in the initial and final weights of the PTEs.

AEMWE assembly and testing

Membrane electrode assembly

The membrane, GDE, and PTE were soaked in fresh 0.5 M KOH for at least 1 h before assembly to ion exchange the residual bicarbonate with hydroxide. The MEA was assembled with a standard Fuel Cell Technology cell. For a 25 cm^2 cell, a 25 cm^2 graphite serpentine flow field on the cathode and a 25 cm^2 nickel serpentine flow field on the anode were used. For a 5 cm^2 cell, the same combination of flow fields was used but masked with ETFE gaskets to obtain a 5 cm^2 active area. When assembling, combinations of 10, 2, and 1 mil ETFE gaskets were used to seal the cell and ensure a 20% compression of the GDE (typically 14 mil on the anode, 13 mil on bare stainless-steel PTL-anode, and 12 mil on the cathode). The cell was tightened to 40 in-lbs at 10 in-lbs increments, following a star pattern. Unless otherwise noted, electrolytes are 0.5 M KOH without any treatments. When heating the cell to 80°C, hot electrolyte liquid (80°C) was fed to the cell until it reached ~50°C, after which cell heater was turned on to maintain the temperature of the cell at 80°C.

Cell testing

The 5 cm^2 cell testing was conducted using a Biologic VSP potentiostat with a 20 A booster (VMP3B-20). Polarization curves were measured via chronopotentiometry without any break-in or activation procedures, and each current was held for 30 s, which was sufficient to reach a steady potential value. The steady-state potential for each current was taken as the average potential over the last 5 s of each current hold. Galvanostatic electrochemical impedance spectroscopy (GEIS) was performed at each current. The signal was modulated by either 5% of the current or 200 mA (lesser of the two), from a frequency of 1 MHz to 1 Hz with ten frequencies per decade. The HFR was determined by determining the higher frequency intercept of GEIS plot with Re(Z) axis. For each cell testing, polarization curves and GEIS of both-fed and dry-cathode conditions were performed on the exact same cell consecutively. Polarization curves and GEIS of both-fed condition were performed first without any break-in or activation procedures. After testing both-fed condition, the catholyte was drained by purging air into catholyte inlet for 5 min using the electrolyte circulation pump. Catholyte inlet was then capped, and outlet was kept open to vent out the produced hydrogen gas to test dry-cathode condition polarization curves and GEIS. For the durability testing, the 25cm^2 cell was tested in dry-cathode condition directly without performing both-fed condition or break-ins first. 25 cm^2 cell testing was conducted using a 200 A booster (FlexP0012).

Three-electrode MEA measurements

For three-electrode MEA measurements, a custom-designed reference cell was attached to the side of the regular MEA cell. A membrane strip was extended out of the MEA cell and into the reference cell, which was used to hold a reference electrode to be in contact with the membrane. A completely leakless Ag/AgCl reference electrode (eDAQ, filling solution 3.4 M KCl) with polyether ether ketone (PEEK) housing was used. According to the manufacturer, the reference electrode is designed to withstand extreme operating conditions such as high pH and elevated temperature.[36] The reference electrode was calibrated against a reversible hydrogen electrode in 1 M hydrochloric acid (pH = 0). The membrane strip provides the necessary ionic connection between the reference electrode and the anode/cathode. No aqueous electrolyte was fed into the reference cell, but the membrane strip was maintained to be well hydrated with DI water to ensure good ionic conductivity. The same cell testing procedure was followed for the three-electrode MEA test as with the two-electrode MEA test. Additionally, it was verified that the three-electrode measurement provided the same full cell measurements as the two-electrode configuration.

For the applied voltage breakdown of the 3-electrode MEA, the thermodynamic equilibrium potentials at reaction conditions (T = 80°C; pH = 13.7) were calculated for the Ag/AgCl reference electrode as well as anode and cathode reactions and used to determine the over potentials on the anode and cathode. Cell voltage, V_{cell}:

$$V_{cell} = V_{cathode} + V_{anode}$$

$$V_{cathode} = \left|E_{HER,80\,^\circ C}\right| + V_{ohmic,cathode} + V_{kinetic,cathode} + V_{residual,cathode}$$

$$V_{anode} = \left|E_{OER,80\,^\circ C}\right| + V_{ohmic,anode} + V_{kinetic,anode} + V_{residual,anode}$$

where E is the thermodynamic potential, and V_{ohmic}, $V_{kinetic}$, and $V_{residual}$ are ohmic, kinetic, and residual overpotentials, respectively.

Electrochemical impedance spectroscopy (EIS) was used to measure the HFR for each electrode. The HFR

was used to calculate the ohmic overpotential based on Ohm's law:

$$V_{ohmic} = i \times R_{HFR} \times A$$

where i [$A\ cm^{-2}$] is the current density, R_{HFR} [Ω] is the resistance obtained from HFR, and A [cm^2] is electrode active area.

Kinetic overpotentials for OER and HER were determined by fitting a Tafel model to the iR-free overpotential below 80 mA/cm^2:

$$\eta = TS \times log_{10}\left(\frac{i}{i_0}\right)$$

where TS [$mV\ dec^{-1}$] is Tafel slope, i [$A\ cm^{-2}$] is current density, and i_0 [$A\ cm^{-2}$] is exchange current density.

The residual overpotential on each electrode was determined by subtracting the thermodynamic equilibrium potential, ohmic overpotential, and kinetic overpotential.

AEMWE durability tests

Durability was performed at a constant current hold. The cell assembly and beginning-of-life polarization curve and impedance measurement were performed as described above. The cell was operated with a dry-cathode configuration (cathode inlet capped off), with a 0.5 M KOH fed to the anode. No break-ins or activation procedures were performed, and the cell was operated with a dry-cathode configuration directly without being operated with a both-fed configuration first. The anolyte reservoir was ~2 L to minimize the impacts of water consumption on KOH concentration. Current was supplied using the Biologic VSP potentiostat with 200 A booster and the cell voltage was recorded by averaging over a period of every 10 min. The electrolyte was replenished with ~30 mL of DI water every 10 min to compensate for water consumption and evaporation and maintain a constant anolyte reservoir volume and KOH concentration during the experiment. After the durability experiment, end-of-life polarization curve was measured on the cell without any treatment.

Hydrogen crossover was monitored periodically during the durability test. Hydrogen crossover was determined by measuring the concentration of hydrogen in the anode oxygen effluent using an SRI Instruments 8610C gas chromatograph equipped with a thermal conductivity detector (TCD). The concentration was averaged over five injections.

Catholyte was also collected periodically during the durability test. Concentration of cations and anions were measured using an IC (DIONEX ICS-6000, Thermo Fisher Scientific) or ICP-mass spectrometry (MS) (ICP-MS 7900, Agilent). For ICP-MS, samples were acidified with ultrapure concentrated nitric acid before injection. A calibration curve ranging from 1 to 1,000 ppb made of a multi-element standard was used for quantification. Multiple internal standards (Sc, Ge) were used to correct for instrumentation drift and matrix effects.

Characterizations

SEM

SEM images were taken using a FEI Quanta FEG 250 under a high vacuum (10^{-5} Torr) with a beam energy of 10 kV. Cross-sectional PTL samples were prepared by casting the sample in a transparent epoxy. After curing, the samples were cross-sectioned, and the surface was polished and deposited with a thin layer of gold for conductivity. Cross-sectional membrane samples were prepared by cracking AEM in liquid nitrogen before SEM imaging.

TEM

For TEM specimen preparation, the electrode samples were scratched off the substrate, dispersed in ethanol through 1-h sonication, and then drop-cast onto lacy carbon-coated TEM copper grids. The bright-field and high-resolution TEM (HRTEM) imaging were performed on an FEI Tecnai F20 operated at 200 keV. High-angle annular dark-field scanning TEM (HAADF-STEM) and EDS mapping were performed on an FEI TitanX 60-300 microscope equipped with a Bruker windowless EDS detector at an acceleration voltage of 300 kV at the National Center for Electron Microscopy at Lawrence Berkeley National Lab.

XPS

XPS were collected using an XPS Kratos Axis Ultra DLD system with a monochromatic Al Kα source (hv = 1,486.6 eV). Spectral analysis was performed using CasaXPS software and binding energies were calibrated to the C 1s signal at 284.8 eV.

X-ray fluorescence spectroscopy

X-ray fluorescence spectra were collected using a Bruker M4 Tornado instrument. The catalyst loading variation was calculated based on the variation in the absolute signal intensity of cobalt.

In situ Raman measurement

Raman spectra were obtained using a confocal Raman microscope (LabRAMHR Evolution, Horiba Jobin Yvon). A commercial Raman cell (Dek Research Instrumentation) was used. A leakless Ag/AgCl reference electrode (eDAQ) with PEEK housing and a platinum wire counter electrode were used. A 50× long working distance objective (LMPLANFL, Olympus, 10.6 mm working distance) was used. A 532 nm laser was used for excitation. Laser was focused on working electrode surface by confirming both charge-coupled device (CCD) camera and laser spot size. The sampling volume is between the working electrode surface and the solution ~1 μm above the surface. Each spectrum was obtained with a 5–10 s acquisition time and 5 accumulations.

Operando X-ray CT measurements and data processing

X-ray CT images were obtained using the micro-CT instrument available at the Advanced Light Source (ALS) 8.3.2 X-ray CT beamline. A white beam mode with a 10× Mitutoyo lens and LuAG 0.5mm scintillator was used to achieve optimal imaging. An exposure time of 40 s with 2,625 back projections were used for each 3D image for OCV conditions and applied currents of 1–3 A/cm^2 with a 3 M CsOH feed on the anode to enhance contrast between electrolyte and gas phase.

ORS Dragonfly was used for stack alignment between different current densities. After stack alignment, the resulting 3D images were processed through ImageJ with Fiji plugin to distinguish between electrolyte and gas phases within the PTLs.

Viscosity measurement

Viscosity measurements were conducted using a rheometer (TA Instruments, Discovery HR-2 Hybrid Rheometer). A 40 mm parallel plate geometry with a solvent trap was used for measurements, with a 700 μm gap.

Particle size and zeta potential measurements

Catalyst ink particle sizes were measured using an acoustic & electro-acoustic spectrometer (Dispersion Technology, DT-1210), which is based upon ultrasound spectroscopy, and enables particle size distribution measurements in concentrated systems. The intrinsic attenuation of the ionomer and solvent system (without catalyst particles) in the range of 1–100 MHz was first measured as a baseline and was then compared with the attenuation of the ink. Attenuation differences as a function of frequency are directly related to particle volume fractions and size distributions and can be fit directly using established methods.[37–39] As part of the calculation, the viscosity of the dispersion solvent was inputted and was measured on the rheometer as described above. Each measurement takes approximately 10 min. Measurements were taken continuously without stirring or shaking the catalyst ink in between measurements. Zeta potentials of the inks were measured immediately after sonication via electrophoretic light scattering (NanoPlus3, Micromeritics, Georgia, USA), modeled using the Smoluchowski equation.[40] Due to the high solid concentration, a 40× dilution of ink was needed to allow light scattering for zeta potential measurement.

Particle size distributions were measured again after storing the ink under static condition for 2 months without any stirring or mixing. Other than hand shaking the ink right before measurement to remove any visible particle settlement, no other mixing techniques were applied during the 2-month period.

RESOURCE AVAILABILITY

Lead contact

Further information and requests for resources and materials should be directed to and will be fulfilled by the lead contact, Xiong Peng (xiongp@lbl.gov) upon request.

Materials availability

There are restrictions to the availability of developed electrodes due to intellectual property ownership. However, authors will accommodate request under agreements.

Data and code availability

The data that support the findings of this study are included in the published article (and its supplemental information) or available from the corresponding author upon request.

ACKNOWLEDGMENTS

R.Y., A.W.T., Y.C., M.C.S., and X.P. would like to thank the project financial support from the Department of Energy, Energy Efficiency and Renewable Energy, Hydrogen and Fuel Cell Technology Office (DOE-EERE-HFTO) under contract number: DE-AC02-05CH11231. S.A.B. and X.P. would also like to thank the HydroGEN Energy Materials Consortium from the Department of Energy, Hydrogen and Fuel Cell Technologies Office for financial support under contract number DE-AC02-05CH11231. Work at the Molecular Foundry was supported by the Office of Science, Office of Basic Energy Sciences, of the US Department of Energy under contract no. DE-AC02-05CH11231. The authors would like to acknowledge that this research used beamline 8.3.2 of the Advanced Light Source, which is a DOE Office of Science User Facility under contract no. DE-AC02-05CH11231. The views expressed in the article do not necessarily represent the views of the DOE or the US Government. All authors would like to thank Dr. Catherine Weiss and Dr. Ramchandra Gawas for helping with inductively coupled plasma mass spectroscopy and ion chromatography measurements, respectively.

AUTHOR CONTRIBUTIONS

R.Y. performed all the ink/electrode fabrication, characterization, cell testing, and data analysis. R.Y. performed ink characterization with support from S. A.B. A.W.T. designed the three-electrode setup and co-developed catalyst ink recipes with R.Y. P.Y. performed *operando* X-ray CT measurement under the supervision of I.V.Z. Y.C. performed TEM analysis under the supervision of M.C.S. X.P. conceived the project. All authors contributed to writing. R.Y. and X.P. were the primary authors of the paper and chiefly responsible for all the experimental design and data analysis.

DECLARATION OF INTERESTS

R.Y., A.W.T., and X.P. declare conflict of interest for an invention disclosure submitted to the Intellectual Property Office at Lawrence Berkeley National Laboratory.

SUPPLEMENTAL INFORMATION

Supplemental information can be found online at https://doi.org/10.1016/j.joule.2025.102001.

Received: April 2, 2025
Revised: May 5, 2025
Accepted: May 22, 2025
Published: June 16, 2025

REFERENCES

1. Guerra, O.J., Zhang, J., Eichman, J., Denholm, P., Kurtz, J., and Hodge, B.-M. (2020). The value of seasonal energy storage technologies for the integration of wind and solar power. Energy Environ. Sci. *13*, 1909–1922. https://doi.org/10.1039/D0EE00771D.
2. Pee, A.d., Pinner, D., Roelofsen, O., and Somers, K. (2018). Decarbonization of industrial sectors: the next frontier (McKinsey & Company). https://www.mckinsey.com/industries/oil-and-gas/our-insights/decarbonization-of-industrial-sectors-the-next-frontier.
3. Deloitte. (2023). Assessment of Green Hydrogen for Industrial Heat. https://www2.deloitte.com/content/dam/Deloitte/us/Documents/Advisory/us-advisory-assessment-of-green-hydrogen-for-industrial-heat.pdf.
4. Cullen, D.A., Neyerlin, K.C., Ahluwalia, R.K., Mukundan, R., More, K.L., Borup, R.L., Weber, A.Z., Myers, D.J., and Kusoglu, A. (2021). New roads and challenges for fuel cells in heavy-duty transportation. Nat. Energy *6*, 462–474. https://doi.org/10.1038/s41560-021-00775-z.
5. Department of Energy. (2023). U.S. National Blueprint for Transportation Decarbonization. https://www.energy.gov/sites/default/files/2023-01/the-us-national-blueprint-for-transportation-decarbonization.pdf.
6. International Energy Agency. (2021). IEA Global Hydrogen Review 2021. https://www.iea.org/reports/global-hydrogen-review-2021.
7. Kusoglu, A. (2021). Chalkboard 1 - The Many Colors of Hydrogen. Electrochem. Soc. Interface *30*, 44–48. https://doi.org/10.1149/2.F12214IF.
8. Ehlers, J.C., Feidenhans'l, A.A., Therkildsen, K.T., and Larrazábal, G.O. (2023). Affordable Green Hydrogen from Alkaline Water Electrolysis: Key Research Needs from an Industrial Perspective. ACS Energy Lett. *8*, 1502–1509. https://doi.org/10.1021/acsenergylett.2c02897.
9. Wang, G., Tricker, A., Lang, J.T., Wang, J., Zenyuk, I., Liu, D.-J., Mukundan, R., and Peng, X. (2024). Understanding Performance Limitation of Liquid Alkaline Water Electrolyzers. J. Electrochem. Soc. *171*, 064501. https://doi.org/10.1149/1945-7111/ad4fe6.
10. Lees, E.W., Bui, J.C., Wang, G., Boyer, H.R., Peng, X., Bell, A.T., and Weber, A.Z. (2024). Modeling the Effect of Material Properties on Liquid-Alkaline Water Electrolysis. J. Electrochem. Soc. *171*, 084502. https://doi.org/10.1149/1945-7111/ad6bc5.

11. Kim, Y., Jung, S.-M., Kim, K.-S., Kim, H.-Y., Kwon, J., Lee, J., Cho, H.-S., and Kim, Y.-T. (2022). Cathodic Protection System against a Reverse-Current after Shut-Down in Zero-Gap Alkaline Water Electrolysis. JACS Au *2*, 2491–2500. https://doi.org/10.1021/jacsau.2c00314.

12. Wang, G., Li, H., Babbe, F., Tricker, A., Crumlin, E.J., Yano, J., Mukundan, R., and Peng, X. (2025). Probing Electrode Transformation under Dynamic Operation for Alkaline Water ElectrolysisPublished online April 17, 2025. Adv. Energy Mater. 2500886. https://doi.org/10.1002/aenm.202500886.

13. Lee, J.K., Anderson, G., Tricker, A.W., Babbe, F., Madan, A., Cullen, D.A., Arregui-Mena, J.D., Danilovic, N., Mukundan, R., Weber, A.Z., et al. (2023). Ionomer-free and recyclable porous-transport electrode for high-performing proton-exchange-membrane water electrolysis. Nat. Commun. *14*, 4592. https://doi.org/10.1038/s41467-023-40375-x.

14. Lee, J.K., Babbe, F., Wang, G., Tricker, A.W., Mukundan, R., Weber, A.Z., and Peng, X. (2024). Nanochannel electrodes facilitating interfacial transport for PEM water electrolysis. Joule *8*, 2357–2373. https://doi.org/10.1016/j.joule.2024.06.005.

15. Wang, C., and Feng, L. (2024). Recent advances and perspectives of Ir-based anode catalysts in PEM water electrolysis. Energy Adv. *3*, 14–29. https://doi.org/10.1039/D3YA00492A.

16. Du, N., Roy, C., Peach, R., Turnbull, M., Thiele, S., and Bock, C. (2022). Anion-Exchange Membrane Water Electrolyzers. Chem. Rev. *122*, 11830–11895. https://doi.org/10.1021/acs.chemrev.1c00854.

17. Li, D., Motz, A.R., Bae, C., Fujimoto, C., Yang, G., Zhang, F.-Y., Ayers, K. E., and Kim, Y.S. (2021). Durability of anion exchange membrane water electrolyzers. Energy Environ. Sci. *14*, 3393–3419. https://doi.org/10.1039/D0EE04086J.

18. Shaik, S., Kundu, J., Yuan, Y., Chung, W., Han, D., Lee, U., Huang, H., and Choi, S.-I. (2024). Recent Progress and Perspective in Pure Water-Fed Anion Exchange Membrane Water Electrolyzers. Adv. Energy Mater. *14*, 2401956. https://doi.org/10.1002/aenm.202401956.

19. Krivina, R.A., Lindquist, G.A., Beaudoin, S.R., Stovall, T.N., Thompson, W.L., Twight, L.P., Marsh, D., Grzyb, J., Fabrizio, K., Hutchison, J.E., et al. (2022). Anode Catalysts in Anion-Exchange-Membrane Electrolysis without Supporting Electrolyte: Conductivity, Dynamics, and Ionomer Degradation. Adv. Mater. *34*, e2203033. https://doi.org/10.1002/adma.202203033.

20. Lim, J., Klein, J.M., Lee, S.G., Park, E.J., Kang, S.Y., Maurya, S., Mustain, W.E., Boettcher, S., and Kim, Y.S. (2024). Addressing the Challenge of Electrochemical Ionomer Oxidation in Future Anion Exchange Membrane Water Electrolyzers. ACS Energy Lett. *9*, 3074–3083. https://doi.org/10.1021/acsenergylett.4c00832.

21. Tricker, A.W., Ertugrul, T.Y., Lee, J.K., Shin, J.R., Choi, W., Kushner, D.I., Wang, G., Lang, J., Zenyuk, I.V., Weber, A.Z., et al. (2024). Pathways Toward Efficient and Durable Anion Exchange Membrane Water Electrolyzers Enabled By Electro-Active Porous Transport Layers. Adv. Energy Mater. *14*, 2303629. https://doi.org/10.1002/aenm.202303629.

22. Chen, B., Biancolli, A.L.G., Radford, C.L., and Holdcroft, S. (2023). Stainless Steel Felt as a Combined OER Electrocatalyst/Porous Transport Layer for Investigating Anion-Exchange Membranes in Water Electrolysis. ACS Energy Lett. *8*, 2661–2667. https://doi.org/10.1021/acsenergylett.3c00878.

23. Li, Z., Lin, G., Wang, L., Lee, H., Du, J., Tang, T., Ding, G., Ren, R., Li, W., Cao, X., et al. (2024). Seed-assisted formation of NiFe anode catalysts for anion exchange membrane water electrolysis at industrial-scale current density. Nat. Cat. *7*, 944–952. https://doi.org/10.1038/s41929-024-01209-1.

24. Magnier, L., Cossard, G., Martin, V., Pascal, C., Roche, V., Sibert, E., Shchedrina, I., Bousquet, R., Parry, V., and Chatenet, M. (2024). Fe–Ni-based alloys as highly active and low-cost oxygen evolution reaction catalyst in alkaline media. Nat. Mater. *23*, 252–261. https://doi.org/10.1038/s41563-023-01744-5.

25. Wang, R., Ohashi, M., Ishida, M., and Ito, H. (2022). Water transport analysis during cathode dry operation of anion exchange membrane water electrolysis. Int. J. Hydrog. Energy *47*, 40835–40848. https://doi.org/10.1016/j.ijhydene.2022.09.181.

26. Tricker, A.W., Lee, J.K., Shin, J.R., Danilovic, N., Weber, A.Z., and Peng, X. (2023). Design and operating principles for high-performing anion exchange membrane water electrolyzers. J. Power Sources *567*, 232967. https://doi.org/10.1016/j.jpowsour.2023.232967.

27. Koch, S., Disch, J., Kilian, S.K., Han, Y., Metzler, L., Tengattini, A., Helfen, L., Schulz, M., Breitwieser, M., and Vierrath, S. (2022). Water management in anion-exchange membrane water electrolyzers under dry cathode operation. RSC Adv. *12*, 20778–20784. https://doi.org/10.1039/D2RA03846C.

28. Huang, G., Mandal, M., Hassan, N.U., Groenhout, K., Dobbs, A., Mustain, W.E., and Kohl, P.A. (2021). Ionomer Optimization for Water Uptake and Swelling in Anion Exchange Membrane Electrolyzer: Hydrogen Evolution Electrode. J. Electrochem. Soc. *168*, 024503. https://doi.org/10.1149/1945-7111/abde7b.

29. Wang, R., Inoguchi, K., Ohashi, M., Someya, S., Munakata, T., Ishida, M., and Ito, H. (2021). Effect of catalyst distribution and structural properties of anode porous transport electrodes on the performance of anion exchange membrane water electrolysis. Int. J. Hydrog. Energy *46*, 37757–37767. https://doi.org/10.1016/j.ijhydene.2021.09.078.

30. Chang, H.-M.J., Firas, N.M., Lang, J.T., Lopez Ochoa, J.A., Stansberry, J. M., Parkinson, D.Y., Karatay, E., Danilovic, N., and Zenyuk, I.V. (2025). Visualizing Oxygen Distribution in the Along-the-channel Direction of Polymer Electrolyte Membrane Water Electrolyzers Using X-ray Imaging. J. Electrochem. Soc. *172*, 014506. https://doi.org/10.1149/1945-7111/ada63c.

31. Li, D., Park, E.J., Zhu, W., Shi, Q., Zhou, Y., Tian, H., Lin, Y., Serov, A., Zulevi, B., Baca, E.D., et al. (2020). Highly quaternized polystyrene ionomers for high performance anion exchange membrane water electrolysers. Nat. Energy *5*, 378–385. https://doi.org/10.1038/s41560-020-0577-x.

32. Olsson, J.S., Pham, T.H., and Jannasch, P. (2018). Poly(arylene piperidinium) Hydroxide Ion Exchange Membranes: Synthesis, Alkaline Stability, and Conductivity. Adv. Funct. Mater. *28*, 1702758. https://doi.org/10.1002/adfm.201702758.

33. Gao, J., Xu, C.-Q., Hung, S.-F., Liu, W., Cai, W., Zeng, Z., Jia, C., Chen, H. M., Xiao, H., Li, J., et al. (2019). Breaking Long-Range Order in Iridium Oxide by Alkali Ion for Efficient Water Oxidation. J. Am. Chem. Soc. *141*, 3014–3023. https://doi.org/10.1021/jacs.8b11456.

34. Chen, G., Zhu, Y., Chen, H.M., Hu, Z., Hung, S.-F., Ma, N., Dai, J., Lin, H.-J., Chen, C.-T., Zhou, W., et al. (2019). An Amorphous Nickel–Iron-Based Electrocatalyst with Unusual Local Structures for Ultrafast Oxygen Evolution Reaction. Adv. Mater. *31*, e1900883. https://doi.org/10.1002/adma.201900883.

35. Padgett, E., Yarlagadda, V., Holtz, M.E., Ko, M., Levin, B.D.A., Kukreja, R. S., Ziegelbauer, J.M., Andrews, R.N., Ilavsky, J., Kongkanand, A., et al. (2019). Mitigation of PEM Fuel Cell Catalyst Degradation with Porous Carbon Supports. J. Electrochem. Soc. *166*, F198–F207. https://doi.org/10.1149/2.0371904jes.

36. eDAQ. Frequently Asked Questions Electrodes. https://www.edaq.com/wiki/Frequently_Asked_Questions_Electrodes#Effect_of_high_pH_values.

37. Dukhin, A.S., and Goetz, P.J. (2001). Acoustic and electroacoustic spectroscopy for characterizing concentrated dispersions and emulsions. Adv. Colloid Interface Sci. *92*, 73–132. https://doi.org/10.1016/S0001-8686(00)00035-X.

38. Dukhin, A.S., and Goetz, P.J. (2002). Ultrasound for Characterizing Colloids. In Studies in Interface Science (Elsevier), v-vi. https://doi.org/10.1016/S1383-7303(02)80011-4.

39. Dukhin, A.S., and Goetz, P.J. (2017). Preface to the Third Edition. In Characterization of Liquids, Dispersions, Emulsions, and Porous Materials Using Ultrasound, Third Edition (Elsevier). https://doi.org/10.1016/B978-0-444-63908-0.05001-8.

40. Berlinger, S.A., McCloskey, B.D., and Weber, A.Z. (2018). Inherent Acidity of Perfluorosulfonic Acid Ionomer Dispersions and Implications for Ink Aggregation. J. Phys. Chem. B *122*, 7790–7796. https://doi.org/10.1021/acs.jpcb.8b06493.